

# The Radial Distribution of Ions and Electrons in RF Inductively Coupled H<sub>2</sub>/T<sub>2</sub>B Plasmas

Xing Ai<sup>1</sup> · Guo Chen<sup>1</sup> · Ling Zhang<sup>1</sup> · Lei Liu<sup>1</sup> · Xiao-Shan He<sup>1</sup> · Zhi-Bing He<sup>1</sup> · Kai Du<sup>1</sup>

Received: 31 May 2017 / Accepted: 19 October 2017 / Published online: 24 October 2017  
© Springer Science+Business Media, LLC 2017

**Abstract** A glow discharge polymer (GDP) was fabricated using trans-2-butene (T<sub>2</sub>B) and hydrogen (H<sub>2</sub>) via a plasma-enhanced chemical vapor deposition (PECVD) system. The uniformity of the GDP films was significantly affected by the radial distribution of the H<sub>2</sub>/T<sub>2</sub>B plasma parameters. The plasma properties while discharging by a multi-carbon gas source of mixed H<sub>2</sub>/T<sub>2</sub>B were investigated during the GDP deposition process. The main positive ions and ion energy distributions in inductively coupled H<sub>2</sub>/T<sub>2</sub>B plasmas were analyzed by energy-resolved mass spectrometer (MS), and the electron density and the effective electron temperature were mainly analyzed using a Langmuir probe. The MS results show that the main positive ions in the plasmas are C<sub>2</sub>H<sub>4</sub><sup>+</sup>, C<sub>2</sub>H<sub>6</sub><sup>+</sup>, C<sub>3</sub>H<sub>3</sub><sup>+</sup>, C<sub>3</sub>H<sub>6</sub><sup>+</sup>, C<sub>3</sub>H<sub>8</sub><sup>+</sup>, C<sub>4</sub>H<sub>5</sub><sup>+</sup>, C<sub>4</sub>H<sub>10</sub><sup>+</sup>, C<sub>5</sub>H<sub>5</sub><sup>+</sup>, and C<sub>5</sub>H<sub>7</sub><sup>+</sup> with mass-to-charge ratios (m/e) of 28, 30, 39, 42, 44, 53, 58, 65, and 67, respectively. For a normalized ion intensity, the relative intensities of saturated CH ions increase with increasing radial distance, while the unsaturated CH ions decrease with increasing radial distance. The ion energy distribution of C<sub>2</sub>H<sub>6</sub><sup>+</sup> (m/e = 30) presents a bimodal structure. Additionally, both the electron density and the effective electron temperature decrease with increasing radial distance.

**Keywords** Inductively coupled plasma · Radial distribution · Langmuir probe · Mass spectrometer

## Introduction

With an amorphous structure, a glow discharge polymer (GDP), is typically used as a nominal ablator in inertial confinement fusion experiments [1–3]. Currently, GDP films are fabricated using plasma-enhanced chemical vapor deposition (PECVD) technology [4, 5],

---

✉ Kai Du  
dukai@caep.cn

<sup>1</sup> Research Center of Laser Fusion, China Academy of Engineering Physics, Mianyang 621999, China

where plasma experiences the processes including the discharge of the gas source, ion transport, and the chemical and physical reactions before deposition on the substrate [6]. In these processes, the plasma characteristics play an important role, especially the radial distribution of the plasma. Therefore, investigation of the plasma parameters and their distributions is necessary, and can provide a solid basis for the optimization of GDP films properties. Extensive researches suggest that the Langmuir probe, mass spectrometer (MS), optical emission spectroscopy (OES), etc., have been served to diagnose the properties of electrons and ions in plasma. However, it is difficult to analyze the complex physical and chemical processes during the discharge of plasma via a sole diagnostic tool [7, 8]. Therefore, combining a Langmuir probe and MS to analyze the parameters of electrons and the formation of the main ions is an appropriate method that can lead to better understanding of the reaction processes and mechanism of the discharge plasma.

Recently, inductively coupled plasma (ICP) sources have been widely utilized to deposit films because of their uniform spatial distribution and high plasma density [9, 10]. The diagnosis and analysis about of ICP has been researched by several groups [11–13]. Lee [14] and Zhou et al. [15] measured the spatial variation of parameters in the inductively coupled Ar plasma. Wegner et al. [16] investigated the mode transition of Ar/O<sub>2</sub> discharge. Zhao et al. [17] observed the parameters of a simple mixture gases of Ar/N<sub>2</sub>/CF<sub>4</sub> on the basis of an Ar plasma. It should be noted that GDP films are fabricated by discharge of trans-2-butene (T<sub>2</sub>B) mixed with hydrogen (H<sub>2</sub>), which contains complex multi-carbon ionic groups and various cracking modes [18]. For these complex gas sources, the influence of technological parameters on the ionic components of the plasma has been studied by our group. It was demonstrated that the dissociation and ionization of H<sub>2</sub>/T<sub>2</sub>B plasmas change with various technological parameters [18, 19]. We confirmed that the radio frequency (RF) power, pressure and flow ratio could significantly affect the surface roughness and morphology of GDP films. Previous results indicated that the optimum conditions for the deposition of GDP films were 15 W, 10 Pa, and a flow ratio of 10/0.4 [20, 21]. Based on these results, it is necessary to explore the radial distribution of the plasma parameters to further improve the qualities of GDP films.

In this paper, a Langmuir probe combined with energy-resolved mass spectrometer are utilized to realize the in situ diagnosis of plasma parameters in the effective film forming area in a H<sub>2</sub>/T<sub>2</sub>B ICP reactor. The effects of radial distance on plasma properties such as plasma potential, electron density and effective electron temperature are discussed. In addition, changes in the formation, relative intensity, and ion energy distributions (IEDs) of the typical hydrocarbon ions with the various radial distances are demonstrated.

## Experimental Details

A RF-PECVD system equipped with a Langmuir probe (ESPion, Hiden Analytical) and energy-resolved MS (PSM 003, Hiden Analytical) was used to realize the in situ diagnosis of the plasma. The experimental setup is illustrated in Fig. 1. A solenoidal copper antenna coil used to sustain discharge, was wound around the wall of a conical quartz tube. The conical quartz tube used as the discharge chamber had a bottom radius of 20 mm and an upper radius of 10 mm, and was extended into the reaction chamber (250 mm in diameter and 315 mm in height). A driving RF of 40.68 MHz (COMDEL, CV-500) was applied to the coil. The mixed gases (active gas: H<sub>2</sub>, precursor gas: T<sub>2</sub>B) were ionized in the conical quartz tube and entered the reaction chamber. The reaction chamber was evacuated to

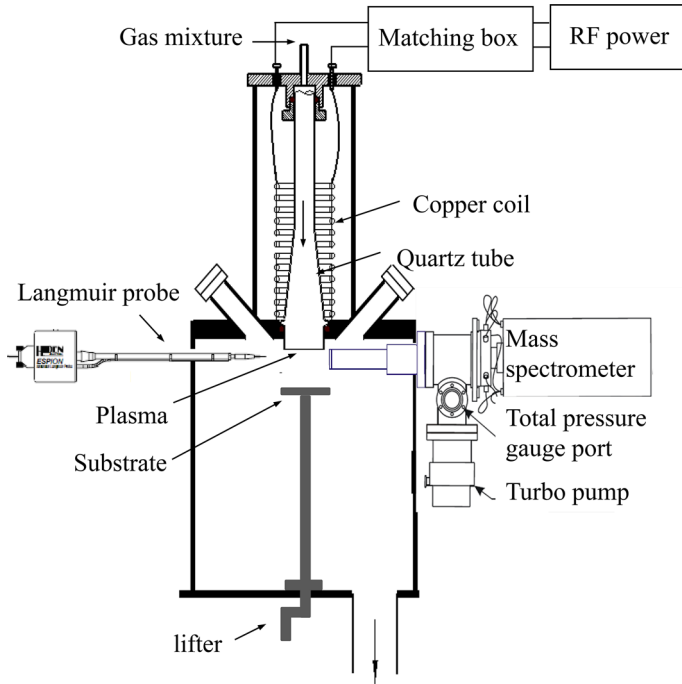


**Fig. 1** Schematic diagram of GDP films deposition and plasma diagnostics

$6.0 \times 10^{-4}$  Pa by a vacuum system including a turbo-molecular pump and a mechanical pump. The inflow rates of  $H_2$  and  $T_2B$  were set at 10 and  $0.4 \text{ cm}^3/\text{min}$ , respectively. The RF power and working pressure were fixed at 15 W and 10 Pa, respectively. Based on our previous work, the above parameters are the optimum parameters for GDP films deposition. Most notably, our PECVD system was built on a low-temperature ICP source with a narrow discharge chamber, thus, the GDP films were deposited in the diffusion region of the plasma.

As shown in Fig. 1, the moveable energy-resolved MS and probe were positioned at 20 mm below the conical quartz tube, which was helpful for obtaining knowledge of the plasma parameters at various radial distances ranging from 0 to 20 mm in the effective film forming area. The distance was considered to be from the center of the substrate to the orifice of the MS or the pinpoint of the probe. We acquired the mass spectra by setting MS in the mode of “+ion SIMS” because the main component of plasma is positive ions during the deposition of the GDP films. The orifice diameter of the MS detector is 100 microns and is bored on the edge of the sampling orifice plate. The accurate range of measurement of mass is 0–300 amu, and that for the ion energy is 0–1000 eV. The Langmuir probe tip is made of tungsten wire. Only a 5 mm segment is exposed to the plasma, and the rest of the probe connection is covered by quartz tubing to shield it from the plasma. The current–voltage (I–V) curves were measured by sweeping the voltage from  $-100$  to  $100$  V. The obtained parameters were the local values around a given point. The I–V curves were obtained at the per unit area on a probe surface per unit time according to the principle of the Langmuir probe. To minimize the error caused by RF interference, a

resonance filter unit was attached to the probe measurement circuit to match the RF frequency (40.68 MHz).

## Results and Discussion

### Dependence of Ion Intensity on the Radial Distance

The growth of GDP films is primarily attributed to hydrocarbon ions, therefore, our investigation focused on these CH ions. The mass spectra obtained at various radial distances in the  $H_2/T_2B$  plasmas are represented in Fig. 2. The typical  $m/e$  peaks and the corresponding ions at different radial distances are shown as follows:  $m/e = 28$  ( $C_2H_4^+$ ),  $m/e = 30$  ( $C_2H_6^+$ ),  $m/e = 39$  ( $C_3H_3^+$ ),  $m/e = 42$  ( $C_3H_6^+$ ),  $m/e = 44$  ( $C_3H_8^+$ ),  $m/e = 53$  ( $C_4H_5^+$ ),  $m/e = 58$  ( $C_4H_{10}^+$ ),  $m/e = 65$  ( $C_5H_5^+$ ),  $m/e = 67$  ( $C_5H_7^+$ ), etc. The strongest and secondary peaks appear at  $m/e = 30$  and  $m/e = 39$ , respectively. In addition, there are many fragment ion peaks near the typical ion peaks, such as  $m/e = 27$  ( $C_2H_3^+$ ),  $m/e = 29$  ( $C_2H_5^+$ ),  $m/e = 41$  ( $C_3H_5^+$ ),  $m/e = 43$  ( $C_3H_7^+$ ),  $m/e = 55$  ( $C_4H_7^+$ ), etc. The appropriate signals for  $C_2H_3^+$ ,  $C_3H_5^+$ , and  $C_4H_7^+$  correspond to mono-olefin molecules; another two peaks for  $C_2H_5^+$ , and  $C_3H_7^+$  are caused by fragment ions of alkane [22]. Clearly, C=C and C–C bonds exist in the major components of  $H_2/T_2B$  plasmas, which is consistent with the results of Fourier Transform Infrared Spectroscopy (FTIR) [20]. As shown in Fig. 2a–e, the hydrocarbon ion densities obviously reduce with the increase of radial distances, which indicates a weakening of the ionization degree.

As can be seen in Fig. 2, the intensity of  $T_2B$  in the spectra is small, which means that the parent molecules ( $T_2B$ ) are mostly dissociated. The  $T_2B$  molecules lose one electron and become into molecule ions through the glow discharge process [19, 23]. It is unstable and would dissociate through collision with energetic electrons or other particles. The possible reactions of  $C_4H_8$  (tran-2-butene,  $T_2B$ ) in the plasma region can be deduced according to the spectra of positive ions in the reaction chamber [24, 25]. Specially, the  $H_2/$

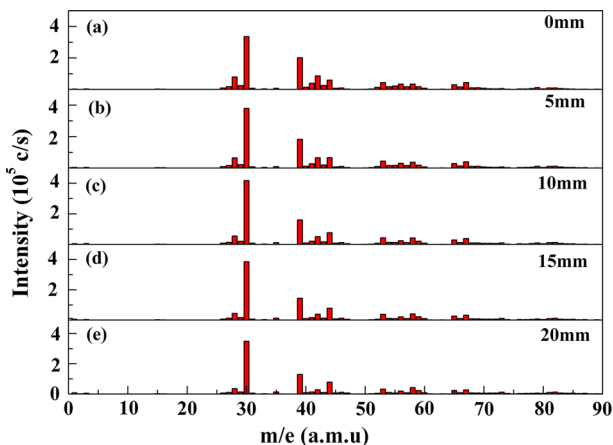
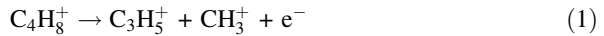


**Fig. 2** Mass spectra of positive ions of  $H_2/T_2B$  plasmas at different radial distances: **a** 0 mm; **b** 5 mm; **c** 10 mm; **d** 15 mm; **e** 20 mm

T<sub>2</sub>B mixture gases discharge contains complex multi-carbon ionic groups and various cracking modes. Thus, we only list some important reactions as follows:

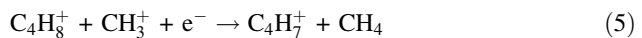
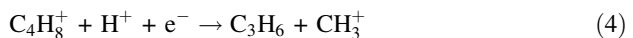
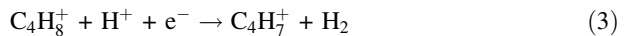
1. C<sub>4</sub>H<sub>8</sub><sup>+</sup> dissociated into allylic (C<sub>3</sub>H<sub>5</sub><sup>+</sup>) and methyl (CH<sub>3</sub><sup>+</sup>) ions via the dissociation of α-C–C bonds [18]:



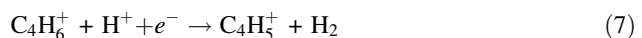
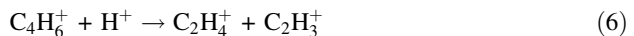
2. C<sub>4</sub>H<sub>7</sub><sup>+</sup> was produced via the dissociation of β-C–H bonds in T<sub>2</sub>B [26]:



3. C<sub>4</sub>H<sub>8</sub><sup>+</sup> molecules ions collided with heavy particles or other ions [19]:



Using these reactions in the plasma region, we can infer the main formation processes of the hydrocarbon ions. The C–C bond energy is lower than that of C–H bonds as  $E(\text{C–C}) = 3.6 \text{ eV} < E(\text{C–H}) = 4 \text{ eV}$  [27]. Therefore, C–C bonds are more prone to be broken by collisions with energetic electrons. Hence, the T<sub>2</sub>B molecules can easily crack into C<sub>3</sub>H<sub>5</sub><sup>+</sup> and CH<sub>3</sub><sup>+</sup>, both of which have high energy. The small hydrocarbon fragment ions are formed by subsequent collisions between electrons and energetic particles in the plasma [19]. For example, the fragment ion C<sub>3</sub>H<sub>5</sub><sup>+</sup> is more likely to dehydrogenate via the bombardment of energetic particles or electrons. The typical positive ion C<sub>3</sub>H<sub>3</sub><sup>+</sup> is produced via continuous breaking of β-H bonds. This is the reason why the intensity of C<sub>3</sub>H<sub>3</sub><sup>+</sup> is quite high in Fig. 2. It also holds true for the fragment ion C<sub>4</sub>H<sub>6</sub><sup>+</sup>. The typical positive ion C<sub>2</sub>H<sub>4</sub><sup>+</sup> ( $m/e = 28$ ) and fragment ion C<sub>2</sub>H<sub>3</sub><sup>+</sup> ( $m/e = 27$ ) are formed by the dissociation of C<sub>4</sub>H<sub>6</sub><sup>+</sup> [28]:



In addition to the main dissociation and ionization reactions presented above, polymerization also occurs in our experiments. The active groups of methyl (CH<sub>3</sub><sup>+</sup>) are formed as a result of dissociation and ionization of the T<sub>2</sub>B or other hydrocarbon ions. These groups can easily be recombined into stable ethane molecules [29]. Hence, one can see from Fig. 2 that the intensity of the typical positive ion C<sub>2</sub>H<sub>6</sub><sup>+</sup> ( $m/e = 30$ ) appears to be significantly high. It is probable that C<sub>3</sub>H<sub>8</sub><sup>+</sup> ( $m/e = 44$ ) is generated via the polymerization of C<sub>2</sub>H<sub>5</sub><sup>+</sup> ( $m/e = 29$ ) with methyl, and C<sub>4</sub>H<sub>10</sub><sup>+</sup> ( $m/e = 58$ ) is generated through the polymerization of C<sub>3</sub>H<sub>7</sub><sup>+</sup> ( $m/e = 43$ ) with methyl [28]. Furthermore, multi-carbon ions are formed by the secondary polymerization of other active groups and methyl, which further reduces the density of methyl [20]. The typical positive ion C<sub>5</sub>H<sub>7</sub><sup>+</sup> ( $m/e = 67$ ) is produced by polymerization of C<sub>4</sub>H<sub>5</sub><sup>+</sup> and CH<sub>3</sub><sup>+</sup>. The subsequent continuous loss of H in C<sub>5</sub>H<sub>7</sub><sup>+</sup> results in the formation of C<sub>5</sub>H<sub>5</sub><sup>+</sup> ( $m/e = 65$ ). As a consequence, the intensity of methyl is not significant at the peak of  $m/e = 15$ , as shown in Fig. 2.

The absolute values of the positive ion intensities are affected by the working parameters of MS analyser, and hence they are not conducive for radial comparison. We therefore normalized the intensity of typical positive ions at various radial distances. Figure 3 presents the normalized relative intensity of different positive ions as they vary with radial distance, in which the normalized relative intensity is calculated as the intensity of each typical positive ion divided by the total intensity of typical positive ions. The relative intensities of the saturated CH ions  $C_2H_6^+$  ( $m/e = 30$ ),  $C_3H_8^+$  ( $m/e = 44$ ), and  $C_4H_{10}^+$  ( $m/e = 58$ ) increase as the radial distance increases in the effective film forming area, which indicates an increased number of C–C bonds. The symbol “↑” in Fig. 3 represents an increase in relative intensity. The relative intensities of the unsaturated CH ions  $C_2H_4^+$  ( $m/e = 28$ ),  $C_3H_3^+$  ( $m/e = 39$ ),  $C_3H_6^+$  ( $m/e = 42$ ),  $C_4H_5^+$  ( $m/e = 53$ ),  $C_5H_5^+$  ( $m/e = 65$ ), and  $C_5H_7^+$  ( $m/e = 67$ ) decrease with increasing radial distance, which indicates an increased number of C=C bonds. The symbol “↓” in Fig. 3 represents a decrease in relative intensity.

These saturated CH ions  $C_2H_6^+$  ( $m/e = 30$ ),  $C_3H_8^+$  ( $m/e = 44$ ), and  $C_4H_{10}^+$  ( $m/e = 58$ ), are mostly generated by the self-polymerization of methyl, and polymerization of methyl with ethyl and propyl, respectively. As the radial distance increases, the ionization decreases and the polymerization increases because the number of energetic electrons decreases (as shown in “Dependence of Electron Parameters on the Radial Distance” section), although the electrons collide with neutral and other charged particles. Thus, the polymerization of methyl increases with increasing radial distance, and the relative intensities of saturated CH ions increase. The number of C–C bonds in saturated CH ions also increases. When organic compounds are ionized by collision with energetic particles, crack centers are generally formed around the C=C or C–C bonds. These bonds are active and in an instable state making them easy to crack spontaneously around the crack center. The order of the electronic energy level is as follows: n-orbital > conjugated  $\pi$ -orbital > individual  $\pi$ -orbital >  $\sigma$ -orbital [22]. This indicates that the C=C bonds in unsaturated CH ions are easier to break around the crack center than C–C bonds. Hence,

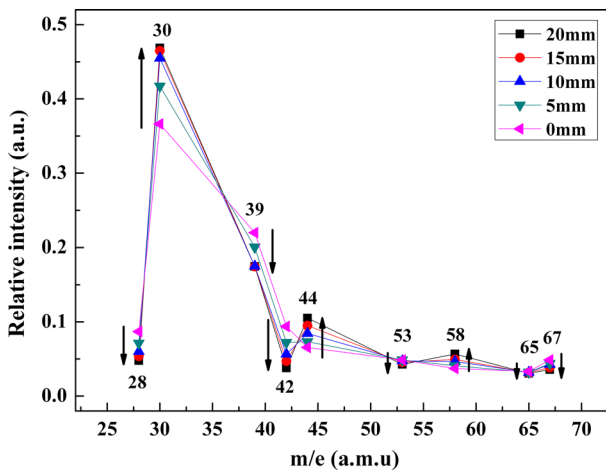


**Fig. 3** Variation of the normalized relative intensities of typical positive ions with radial distance. The symbol “↑” indicates that the relative intensity increases, which is opposite that of the downward arrow “↓”

spontaneous cracking around the crack center is the main reason for C=C double bond breaking.

The CH ion carries more energy with increasing radial distance, as shown in “[Dependence of Ion Energy Distributions on the Radial Distance](#)” section, which make the unsaturated CH ions become more instable and crackable as the radial distance increases. Meanwhile, unsaturated olefin radicals are soon saturated because of the strong tendency of electron pairing, after which alkane ions are formed. Therefore, the relative intensities of saturated CH ions further increase as the radial distance increases, while the unsaturated CH ions, including  $C_2H_4^+$  ( $m/e = 28$ ),  $C_3H_3^+$  ( $m/e = 39$ ),  $C_3H_6^+$  ( $m/e = 42$ ), and  $C_4H_5^+$  ( $m/e = 53$ ), fall, as shown in Fig. 3. Moreover, the relative intensities of the unsaturated polymer ions  $C_5H_5^+$  ( $m/e = 65$ ) and  $C_5H_7^+$  ( $m/e = 67$ ), which are produced by the secondary polymerization, decrease. Although the polymerization increases, multi-carbon polymers are prone to cracking due to their inherent instability, as discussed above [26]. It can be concluded that the number of C–C bonds gradually increases as the radial distance increases, while the number of C=C bonds decreases.

### Dependence of Ion Energy Distributions on the Radial Distance

The ion energy distributions (IEDs) play a valuable part in the structure, morphology, and surface roughness of GDP films during the deposition process. It is important to discuss the energy distribution of typical hydrocarbon ions at different radial distances. Because of the similar IEDs of CH ions, only the curves of the typical positive ion  $C_2H_6^+$  for different radial distances are plotted in Fig. 4, which were measured by energy-resolved mass spectrometer. All of the measured IEDs curves exhibit a bimodal distribution at various radial distances, and the bimodal shape becomes increasingly obvious with increasing radial distance.

While the frequency is high ( $\tau_{ion}/\tau_{rf} \gg 1$ ), the ions cross the sheath between the plasma and plasma vessel walls through enough rf cycles, which leads to ions movement being controlled by the time-averaged ambipolar potential, and the ion motion is therefore not

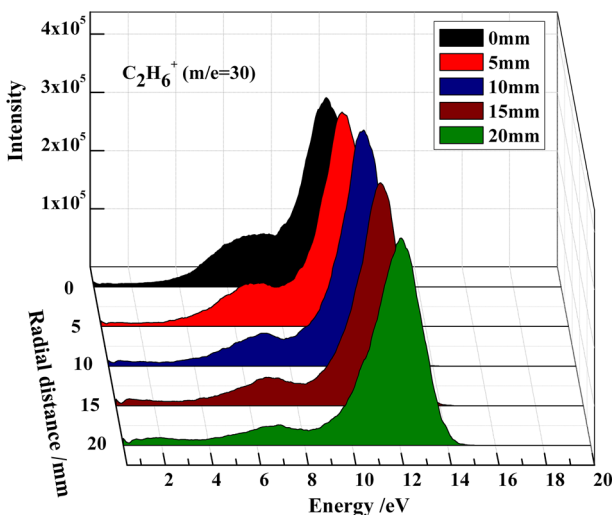


**Fig. 4** Ion energy distributions curves for  $m/e = 30$  at different radial distances

affected by the instantaneous RF field [30, 31]. However, the IEDs curves in Fig. 4 were obtained at the expansion region, in which the ions accelerate between the conical quartz tube and the reaction chamber. While considering the shapes of IEDs for ions in plasma, it is necessary to consider the formation mechanism of ions. It is well known that the electron collide with other particles, which is the primary reason for the initial formation of ions, and the ions can also obtain energy through the collision [32]. There are many collision processes, as discussed above in the case of complex gas mixtures during ion acceleration in the expansion region [33]. Thus, ion-neutral collisions typically result in broad energy distributions that contain multiple peaks [32]. Another notable characteristic of these IEDs is that the high energy peak ( $E_1$ ) increases gradually from 10.15 to 12.05 eV, and the low energy peak ( $E_2$ ) shifts from 7.5 to 6.9 eV. The maximum sheath potential ( $\Delta E = E_1 - E_2$ ), which stretches across the gap between the two peaks, increases with increasing radial distance. The bimodal shape becomes increasingly obvious with increasing radial distance, as shown in Fig. 4. It is contributed to that part of ions transit the sheath between the plasma and the entrance slit of the mass-spectrometer without collision, which leads to a reduction in energy loss, and the low energy component dissipates as the radial distance increases [30].

### Dependence of Electron Parameters on the Radial Distance

Electron density and effective electron temperature play a vital role in discussing the composition and state of a plasma. To calculate these parameters for the  $H_2/T_2B$  plasma in the diffusion region, the second derivatives of the I–V curves ( $I''$ ) were obtained by numerical smoothing and differentiation. The zero crossing point of  $I''$  indicates the value of plasma potential ( $V_p$ ). The proportional relationship between  $I''$  and the electron energy distribution functions (EEDF) is indicated by Eq. (8) [34]:

$$F(\varepsilon) = \frac{2m}{e^2 A} \left( \frac{2eV}{m} \right)^{1/2} I'' \quad (8)$$

where  $F(\varepsilon)$ ,  $m$ ,  $e$ , and  $A$  denote and EEDF, electron mass, electron charge, and area of the probe, respectively. The electron density  $n_e$  and the effective electron temperature  $T_{\text{eff}}$  are integrated from the EEDF, as shown in Eqs. (9) and (10), respectively:

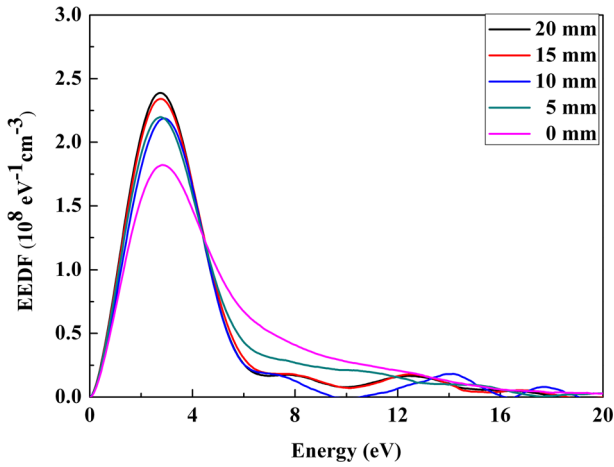
$$n_e = \int_0^{\infty} F(\varepsilon) d\varepsilon \quad (9)$$

$$T_{\text{eff}} = \frac{2}{3n_e} \int_0^{\infty} \varepsilon F(\varepsilon) d\varepsilon \quad (10)$$

In our experiments, the plasmas are generated by a copper antenna coil with a diameter of 60 mm, which is smaller than the reaction chamber, which has a diameter of 250 mm.

The measured EEDF curves for different values of radial distance are plotted in Fig. 5. The fraction of low-energy electrons increased, while the fraction of high-energy electrons decreased with increasing radial distance. These results indicate that the high-energy electron exchanges energy with other particles around the coil, and the energy decreases with increasing radial distance [17, 35]. The EEDF can be used to calculate the electron density and the effective electron temperature, as shown in Figs. 7 and 8, respectively.



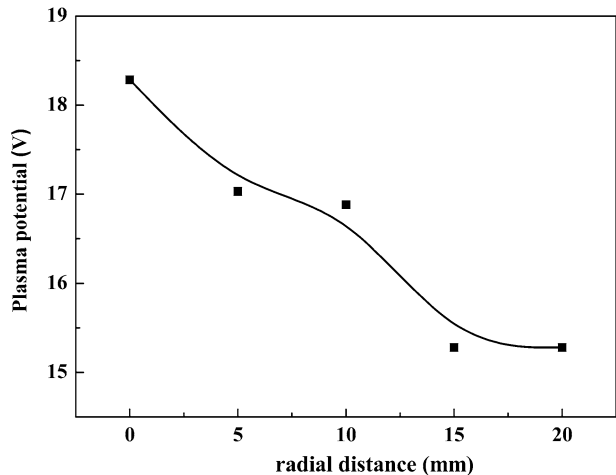


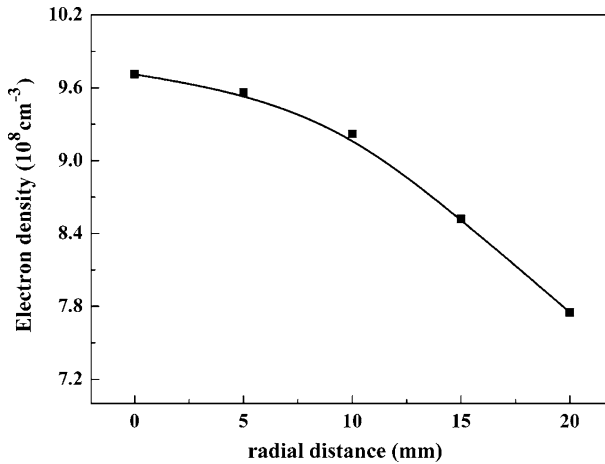
**Fig. 5** Variation of the electron energy distribution function (EEDF) with radial distance

Figure 6 shows the variation of the plasma potential ( $V_p$ ) with radial distance. As can be seen in Fig. 6, the  $V_p$  has a maximum at 0 mm radial distance due to the ambipolar diffusion. The value of  $V_p$  is determined by the high-energy electrons [15], and the fraction of high-energy electrons decreased with increasing radial distance as shown in Fig. 5. As a result, the value of  $V_p$  decreases with increasing radial distance. The ions are accelerated to the walls while the electrons need to overcome the potential during the radial diffusion due to the ambipolar potential. Thus, the electrons get the highest kinetic energy at 0 mm radial distance and are decelerated from center of the substrate to boundary [36].

Figure 7 shows the variation of the electron density ( $n_e$ ) with radial distance. The radial distance has an impact on  $n_e$ , and its value decreases from  $9.71 \times 10^8 \text{ cm}^{-3}$  at 0 mm to  $7.75 \times 10^8 \text{ cm}^{-3}$  at 20 mm, as can be seen in Fig. 7. It is well known that there are two discharge modes in ICP, including a capacitive coupled mode (E mode) and an inductive coupled mode (H mode). The transition of the E mode to the H mode occurs as the RF

**Fig. 6** Variation of plasma potential with radial distance





**Fig. 7** Variation of electron density with radial distance

power increases. The range of electron density is usually  $10^{10}$ – $10^{12} \text{ cm}^{-3}$  for the typical H mode discharge, and it is  $10^8$ – $10^9 \text{ cm}^{-3}$  for E mode discharge in ICP [37]. Thus, we estimate that the discharge in our work is the E mode of ICP. As shown in Fig. 7, the maximum  $n_e$  value is obtained at 0 mm. This may be attributed to the high kinetic energy and the strong effect of ionization at the center of the substrate caused by the ambipolar potential as discussed in Fig. 6 [36]. In the effective film forming area, the ionization contributes to the generation of electrons, which decrease with increasing radial distance. On the contrary, the consumption of electrons is mostly caused by the complex reactions between electrons and ions. As the radial distance increases, the tendency of the complex reactions in the effective film forming area is reinforced because the ions are accelerated from the center to the edge of the substrate, which leads to more loss of electrons [38]. Thus, the generation of electrons is decreased and the consumption of electron is increased, leading to the  $n_e$  decreases with increasing radial distance.

**Fig. 8** Variation of effective electron temperature with radial distance

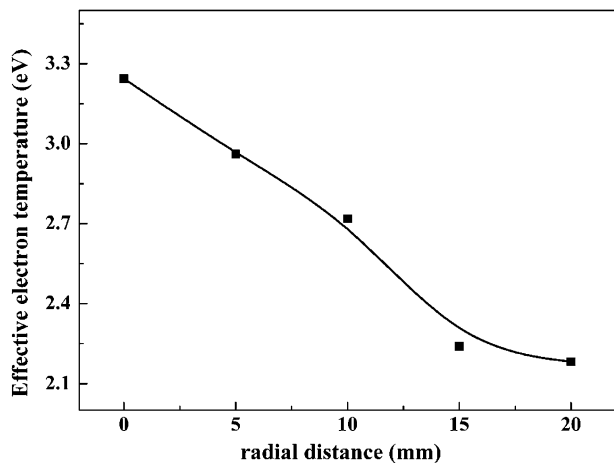


Figure 8 presents the variation of the effective electron temperature  $T_{\text{eff}}$  with radial distance. The  $T_{\text{eff}}$  can be described by the average electron energy ( $\bar{\varepsilon} = \frac{3}{2}kT_{\text{eff}}$ ). In our experimental system, the ICP discharge is driven by an applied RF electric field, where the electrons obtain their input power through RF power transfer. It is interesting that the  $T_{\text{eff}}$  shown in Fig. 8 reaches the maximal value of 3 eV at 0 mm, showing the same trend as the result in Ref. [39]. In this experiment, the working pressure was kept at 75 mTorr (10 Pa), the classical skin depth can be calculated by Eq. (11) [40]:

$$\delta = \delta_0 / \cos(\varepsilon/2) \quad (11)$$

where  $\delta_0 = \frac{c}{\omega_p} \left(1 + \frac{v_{en}^2}{\omega^2}\right)^{1/4}$ ,  $\varepsilon = \tan^{-1}(v_{en}/\omega)$ ,  $c$  is the velocity of light,  $\omega_p$  is the electron plasma frequency,  $\omega$  is the driving frequency,  $v_{en}$  is the collision frequency between electrons and neutral. According to the results in Figs. 7 and 8, the estimate for skin depth  $\delta$  is 5.4 cm, which is larger than the radius of the reactor  $R$  (2 cm). Thus, the skin layers overlap in the discharge reactor. In other words, the RF field punctures the discharge gases, and the RF power is also strong at the center of the substrate. At 10 Pa, the plasma heating mechanism is dominated by ohmic heating, and the heated electrons present a regime of local kinetics, where the energetic electrons can easily lose their energy because of collisions between the electrons and heavy particles [41]. As the radial distance increases, the total number of collisions increases as the electron moving to the edge of the substrate. Therefore, the energetic electrons lose more energy and  $T_{\text{eff}}$  slightly decreases as the radial distance increases. Significantly, the influence of secondary electrons produced through collision can be ignored because the kinetic energy is low.

## Conclusions

In this study, the effect of radial distance on the plasma parameters of ICP discharge in  $\text{H}_2/\text{T}_2\text{B}$  plasmas was investigated using a Langmuir probe and MS. The main positive ions in  $\text{H}_2/\text{T}_2\text{B}$  plasmas after ionization are  $\text{C}_2\text{H}_4^+$  ( $m/e = 28$ ),  $\text{C}_2\text{H}_6^+$  ( $m/e = 30$ ),  $\text{C}_3\text{H}_3^+$  ( $m/e = 39$ ),  $\text{C}_3\text{H}_6^+$  ( $m/e = 42$ ),  $\text{C}_3\text{H}_8^+$  ( $m/e = 44$ ),  $\text{C}_4\text{H}_5^+$  ( $m/e = 53$ ),  $\text{C}_4\text{H}_{10}^+$  ( $m/e = 58$ ),  $\text{C}_5\text{H}_5^+$  ( $m/e = 65$ ) and  $\text{C}_5\text{H}_7^+$  ( $m/e = 67$ ). The formation of these CH ions was analyzed. It is found that with increasing radial distance, the relative intensities of saturated CH ions increased and those of unsaturated CH ions decreased, which demonstrates increasing C–C bonds and decreasing C=C bonds. Another significant finding concerning the positive ions is that the bimodal IEDs of the typical hydrocarbon ion  $\text{C}_2\text{H}_6^+$  obviously changed with increasing radial distance. Moreover, both the electron density and the effective electron temperature decreased with increasing radial distance in the effective film forming area. To sum up, ions migration occurs with bond cracking in the process of plasma diffusion from the center to the edge. We believe that the dissociation of the  $\text{H}_2/\text{T}_2\text{B}$  mixture gases primarily occurs through dissociation and ionization, after which CH fragments are lost because of the cracking of C–C or C–H bonds. These CH fragments are generated to deposit the GDP films with a radial distribution. These results provide a theoretical foundation for understanding the mechanism of plasma composition and state of  $\text{H}_2/\text{T}_2\text{B}$  plasma on the radial growth of GDP films.

**Acknowledgements** This study was funded by the National Natural Science Foundation of China (Grant Number 11504350). The authors are grateful to Yan-Song Liu, Jing-Lin Huang and Cui-Lan Tang who offered the suggestions.

## References

1. Plisson T, Colinlalu P, Huser G, Loubeyre P (2016) *J Appl Phys* 120:085903
2. Reynolds H, Baxamusa S, Haan SW, Fitzsimmons P, Carlson L, Farrell M, Nikroo A, Watson BJ (2016) *J Appl Phys* 119:085305
3. Yan JC, He ZB, Wei JJ, Zhang Y, Zhang L, Tang YJ (2011) *Diam Relat Mater* 20:1042–1045
4. Theobald M, Baclet P, Legaie O, Durand J (2001) *J Vacuum Sci Technol A* 19:118–123
5. He ZB, Yang ZL, Yan JC, Song ZM, Lu TC (2011) *Acta Phys Sin* 60:538
6. Robertson J (2002) *Mater Sci Eng R* 37:129–281
7. Ishpal, Kumar S, Dwivedi N, Rauthan CMS (2012) *Phys Plasmas* 19:033515
8. Vizireanu S, Stoica SD, Luculescu C, Nistor LC, Mitu B, Dinescu G (2010) *Plasma Sources Sci Technol* 19:034016
9. Frischmuth T, Schneider M, Maurer D, Grille T, Schmid U (2016) *Sens Actuators A Phys* 247:647–655
10. Wei DY, Xiao SQ, Huang SY, Chan CS, Zhou HP, Xu LX, Guo YN, Chai JW, Wang SJ, Xu S (2013) *J Phys D Appl Phys* 46:215501
11. Setareh M, Farnia M, Maghari A, Bogaerts A (2014) *J Phys D Appl Phys* 47:355205
12. Mattei S, Nishida K, Mochizuki S, Grudiev A, Lettry J, Tran MQ, Hatayama A (2016) *Plasma Sources Sci Technol* 25:065001
13. Yoo SW, You SJ, Kim JH, Seong DJ, Seo BH, Hwang NM (2017) *J Phys D Appl Phys* 50:035201
14. Lee HC, Chung CW (2012) *Phys Plasmas* 19:033514
15. Zhou LF, Chen J, Ma JH, Li Y (2015) *Vacuum* 119:209–213
16. Wegner T, Küllig C, Meichsner J (2016) *Phys Plasmas* 23:023503
17. Zhao SX, Gao F, Wang YN, Bogaerts A (2012) *Plasma Sources Sci Technol* 21:1257–1261
18. Li R, He ZB, He XS, Niu ZC, Yang XD (2012) *Acta Phys Sin* 61:215203
19. Li R, He ZB, Yang XD, He XS, Niu ZC, Jia XQ (2013) *Acta Phys Sin* 62:058104
20. Zhang L, He XS, Chen G, Wang T, Tang YJ, He ZB (2016) *Appl Surf Sci* 366:499–505
21. Chen G, Zhang L, He XS, He ZB, Tang YJ (2016) *At Eng Sci Technol* 50:1658
22. Li RQ (2005) *Spectral analysis of organic structure*. Tianjin University Press, Tianjin, pp 301–357
23. Hudson CE, Wang D, McAdoo DJ (2004) *Int J Mass Spectrom* 236:105–116
24. Kiefer JH, Gupte KS, Harding LB, Klippenstein SJ (2009) *J Phys Chem A* 113:13570–13583
25. Hittle LR, Hercules DM (1994) *Surf Interface Anal* 21:217–225
26. Zhang YJ, Cai JH, Zhao L, Yang JZ, Jin HF, Cheng ZJ, Li YY, Zhang LD, Qi F (2012) *Combust Flame* 159:905–917
27. Bauer M, Schwarz-Selinger T, Jacob W, Von Keudell A (2005) *J Appl Phys* 98:073302
28. Denysenko IB, Xu S, Long JD, Rutkevych PP, Azarenkov NA, Ostrikov K (2004) *J Appl Phys* 95:2713–2724
29. Li K, Gabriel O, Meichsner J (2004) *J Phys D Appl Phys* 37:588–594
30. Kawamura E, Vahedi V, Lieberman MA, Birdsall CK (1998) *Plasma Sources Sci Technol* 8:45–64
31. Zhang YT, Kushner MJ, Moore N, Pribyl P (2013) *J Vacuum Sci Technol A* 31:061311–061317
32. Martin IT, Zhou J, Fisher ER (2006) *J Appl Phys* 100:013301
33. Olevanov M, Proshina O, Rakhimova T, Voloshin D (2008) *Phys Rev E* 8:026404
34. Druyvesteyn MJ, Penning FM (1940) *Rev Mod Phys* 12:87–174
35. Mao M, Dai ZL, Wang YN (2007) *Plasma Sci Technol* 9:30–34
36. Lee HC, Chung CW (2013) *Phys Plasma* 20:101607
37. Wegner T, Küllig C, Meichsner J (2017) *Plasma Sources Sci Technol* 26:025007
38. Gao F, Mao M, Ding ZF, Wang YN (2008) *Acta Phys Sin* 57:5123
39. Todorov D, Shivarova A, Paunskata T, Tarnev K (2015) *Phys Plasma* 22:033504
40. Kolobov VI, Economou DJ (1997) *Plasma Sources Sci Technol* 6:R1–R17
41. Lee HC, Lee MH, Chung CW (2010) *Appl Phys Lett* 96:041503